PHYSICAL REVIEW B VOLUME 33, NUMBER 4 15 FEBRUARY 1986

Pseudosurface wave structures in phonon imaging

A. G. Every
Department of Physics, University of the Witwatersrand, Johannesburg 2001, South Africa
(Received 16 September 1985)

A parameter-free model for calculating surface directivity effects in phonon images is described. It treats the coupling between crystal and metal-heater and -detector films as an isotropic dissipative mechanism, and it is applicable to situations where the overlayer is of low acoustic impedance or weakly bonded to the crystal substrate. Our calculated phonon-intensity diagrams display well-defined structures which derive from pseudosurface waves (PSW's) in the quasifree crystal surface. These waves differ from Rayleigh waves in that they contain a small bulk-wave component through which they can be excited and into which they decay. Some of these PSW's are closely associated with exit and reentrant critical cones for mode conversion at the crystal surface. In some cases the PSW's evolve, in limiting directions, into true surface waves immersed in a continuum of bulk waves. Phonon imaging is shown to be a useful technique for studying these complex and interesting resonant vibrations in crystal surfaces, and this enhances the potential value of this technique as a sensitive probe of crystal surfaces and interfaces.

I. INTRODUCTION

Pseudosurface waves were first encountered in ultrasonic reflectivity[1,2] and surface-acoustic-wave[3,4] experiments. Nowadays they feature in the interpretation of the elastic scattering of light, molecular beams, and electrons from solid surfaces and interfaces.[5–7] The theoretical properties of these waves have attracted a fair amount of attention.[8–12] In contrast to generalized Rayleigh waves (GRW's), which are true surface waves, pseudosurface waves (PSW's) contain a small bulk-wave component which radiates the energy of the wave into the substrate, and causes the PSW's to attenuate with distance—hence the term "leaky surface waves." Moreover, PSW's can be excited by bulk waves impinging on the surface from the substrate, whereas GRW's, in the absence of anharmonicity and surface imperfection, can only be excited by external means. In the past, little attention was paid to the internal excitation and decay of PSW's. Recent advances in phonon imaging[13] have, however, provided a direct means of observing the complex radiation and excitation pattern of PSW's and deriving from it useful information concerning surface conditions. Koos *et al.*[14] and Every *et al.*[15] have reported on well-defined structures in the phonon images of highly polished sapphire single crystals that arise from longitudinal-type PSW's in the sapphire-metal interface. They infer from their observations that the sapphire surface is flat on the scale of the dominant phonon wavelength and that the coupling to the metal overlayer is considerably weaker than expected on the basis of simple acoustic-mismatch theory. Hurley *et al.*[16] have reported on similar structures in the phonon images of a polished diamond. With suitably shaped samples, allowing large angle views, and appropriate surface preparation, one can expect PSW structures to be a general feature in most phonon images.

In this paper we describe some of the characteristic PSW structures anticipated for a variety of different crystal surfaces. Some of these PSW's have been identified before by Lim and Farnell[9] and other investigators,[1–5] some we draw attention to here for the first time. There is a great wealth of such structures, and although they can be fairly broad, most are sharp to extremely sharp, and so should be clearly discernible in experimental images. It is interesting to note that the topological features of the acoustic-slowness surface that are responsible for bulk-phonon-focusing singularities are also often implicated in the formation of PSW structures. Many of the PSW structures we will be reporting on occur close to critical cones for mode conversion at crystal surfaces.

Our model is based on the premise of a quasifree crystal surface, i.e., a surface which is loaded with a solid medium of low acoustic impedance or, to the same effect, one which is weakly bonded to its adjacent medium. Our calculations assume that a phonon in a bulk mode of the crystal has a transmission probability across the interface which is proportional to the squared amplitude of vibration caused in the free-crystal surface by that (normalized) mode impinging on it. Every *et al.*[15] and Hurley *et al.*[16] have carried out extensive calculations on a variety of metal crystal interface combinations and have found generally that under quasifree conditions PSW resonances that occur in the angular dependence of the phonon emissivity and absorptivity closely resemble corresponding resonances in the squared amplitude of vibration in the free-crystal surface. When the adjacent medium is of high acoustic impedance and perfectly bonded to the crystal substrate, on the other hand, the PSW resonances are almost completely suppressed. While those calculations did assume elastic isotropy, there is no reason to expect the result to be radically affected by the introduction of anisotropy. Experimental support for these ideas is provided by the observation of Every *et al.*[15] that varying the composition of the metal-heater film had no significant effect on their phonon images of sapphire.

Our calculations concern long-wavelength thermal pho-

©1986 The American Physical Society

nons and are carried out in the context of continuum elasticity theory. Known elastic constants of crystals are used, but there are no free parameters in the model. Piezoelectric stiffening of the elastic constants is not considered.

II. METHOD OF CALCULATION

The spatial variation of phonon intensity in phonon images derives principally from two sources: phonon focusing, which is the result of bulk elastic anisotropy, and surface-directivity effects at the heater and detector interfaces. In general, the directionally dependent phonon emissivity and absorptivity at these surfaces depend in a complicated way on the elastic properties of the crystal substrate and metal overlayer,[17] and also on the precise nature of the boundary conditions. Extensive calculations by Every *et al.*[15] and Hurley *et al.*[16] indicate, however, that when the bonding at the interface is weak, or the metal overlayer is of low acoustic impedance, the angular dependence of the phonon emissivity and absorptivity in the crystal become, to a large degree, independent of the precise form of the boundary conditions and the specific properties of the overlayer. Moreover, under these conditions the overlayer appears to act as a simple isotropic dissipative mechanism in that the angular dependence of the emissivity and absorptivity closely resembles that of the squared amplitude of the vibration caused by (normalized) modes impinging on the free-crystal surface. This is the pivotal idea on which our calculations rest. It should be cautioned that in the case of liquid loading only the normal components of the displacement and traction force are transmitted into the overlayer,[18] and so the dissipative mechanism only involves the one component of surface displacement. This has the effect of concealing PSW's whose displacements are predominantly parallel to the surface. In extreme cases solid-solid interfaces can mimic these conditions. Similar considerations apply to light scattering at surfaces.[5]

The PSW structures we describe in this paper therefore apply in the limit of weak surface loading. As the loading becomes greater, in general one can expect the PSW structures to become progressively broader and weaker and eventually completely washed out. Indeed, it is possible, as Every *et al.*[15] have shown, to use the softening of these resonances to obtain a measure of the strength of the bonding between the metal film and crystal substrate.

We proceed by recalling that the equation of motion for an elastically anisotropic solid admits plane-wave solutions of the form

$$\mathbf{u}=\mathbf{U}\exp[i\omega(\mathbf{S}\cdot\mathbf{r}-t)]\ , \tag{1}$$

for the displacement field $\mathbf{u}$. Here, $\mathbf{r}$ and t are position and time, respectively, ω is the angular frequency, $\mathbf{U}$ is the polarization vector, and $\mathbf{S}=(S_x,S_y,S_z)$ is the acoustic-slowness vector ($=\mathbf{k}/\omega$, $\mathbf{k}$ the wave vector). The secular equation[19,20]

$$\Omega(\mathbf{S})=|\,C_{rlsm}S_lS_m-\rho\delta_{rs}\,|=0\ , \tag{2}$$

is of degree 6 in the components of $\mathbf{S}$, C_{rlsm} being the second-order elastic-constant tensor, ρ the mass density, and δ_{rs} the δ function.

We take the crystal surface to be located in the (x,y) plane with the z axis pointing into the interior of the crystal. For any given value of $\mathbf{S}_{\parallel}=(S_x,S_y)$, the projection of $\mathbf{S}$ in this plane, Eq. (2) fixes the value of the third component S_z. The polarization vector for each mode is then obtained by solving the linear equations

$$(C_{rlsm}S_lS_m-\rho\delta_{rs})U_s=0\ . \tag{3}$$

Since Eq. (2) is of degree 6, there are six solutions $S_z^{(j)}$, $j=1,\ldots,6$, defining six waves which phase-match in the crystal surface. For small $|\mathbf{S}_{\parallel}|$ these solutions are all real and the six vectors $\mathbf{S}^{(j)}=(S_x,S_y,S_z^{(j)})$ lie on a surface of three sheets known as the slowness surface.[18-20] These real solutions correspond to homogeneous bulk waves. Three of these waves are approaching the surface, i.e., have ray vectors[18-20] (energy flux vectors)

$$\mathbf{V}=\frac{\nabla_s\Omega(\mathbf{S})}{\mathbf{S}\cdot\nabla_s\Omega(\mathbf{S})}\ , \tag{4}$$

directed toward the surface, and the other three are receding from the surface, i.e., have $\mathbf{V}$ directed into the bulk. Because of elastic anisotropy the $\mathbf{S}$ and $\mathbf{V}$ vectors of a wave are noncollinear, and it is quite common to find $\mathbf{V}$ pointing toward a surface while $\mathbf{S}$ is pointing away, and *vice versa*.

As $|\mathbf{S}_{\parallel}|$ is increased, pairs of real solutions (one incoming wave, one outgoing) merge to be replaced by pairs of complex-conjugate solutions. This occurs at extremal points on the slowness surface where $\mathbf{V}$, which is normal to this surface, is parallel to the (x,y) plane. The loci of points in the (S_x,S_y) plane where such changeovers occur we will call critical contours. The remaining real values of $\mathbf{S}$, which project onto these contours, lie on the $\mathbf{S}$-space critical cones for mode conversion at the crystal surface. Anisotropic media also permit reentrant critical cones at which pairs of complex-conjugate solutions cross over to being real again as $|\mathbf{S}_{\parallel}|$ is increased.[21] Ultimately for large $|\mathbf{S}_{\parallel}|$ all solutions are complex.

By way of example, Fig. 1 shows the slowness surface for CdTe. For this and subsequent calculations, unless otherwise specified, all elastic constant have been taken from Ref. 22. The (S_x,S_y) plane is a mirror-symmetry plane of the crystal and so Eq. (2) reduces to a bicubic equation in S_z. Real solutions therefore occur in equal and opposite pairs, and the slowness surface is symmetric about the (S_x,S_y) plane. The innermost longitudinal (L) sheet is entirely convex[23] and meets this plane at right angles. The line of intersection therefore coincides with the critical contour and is shown by the heavy line. The associated $\mathbf{V}$-space critical cones for the other two branches are composed of rays emanating normally from the slowness surface along the dashed lines labeled L on the other two sheets. The fast transverse (FT) sheet displays broad shallow furrows centered on the cube planes. As a consequence, there are two critical contours for this branch. The first coincides with the line of intersection of this sheet with the (S_x,S_y) plane and is a reentrant contour. Just beyond this line there are again six real solutions. Dashed lines labeled FT on this and the third sheet indi-

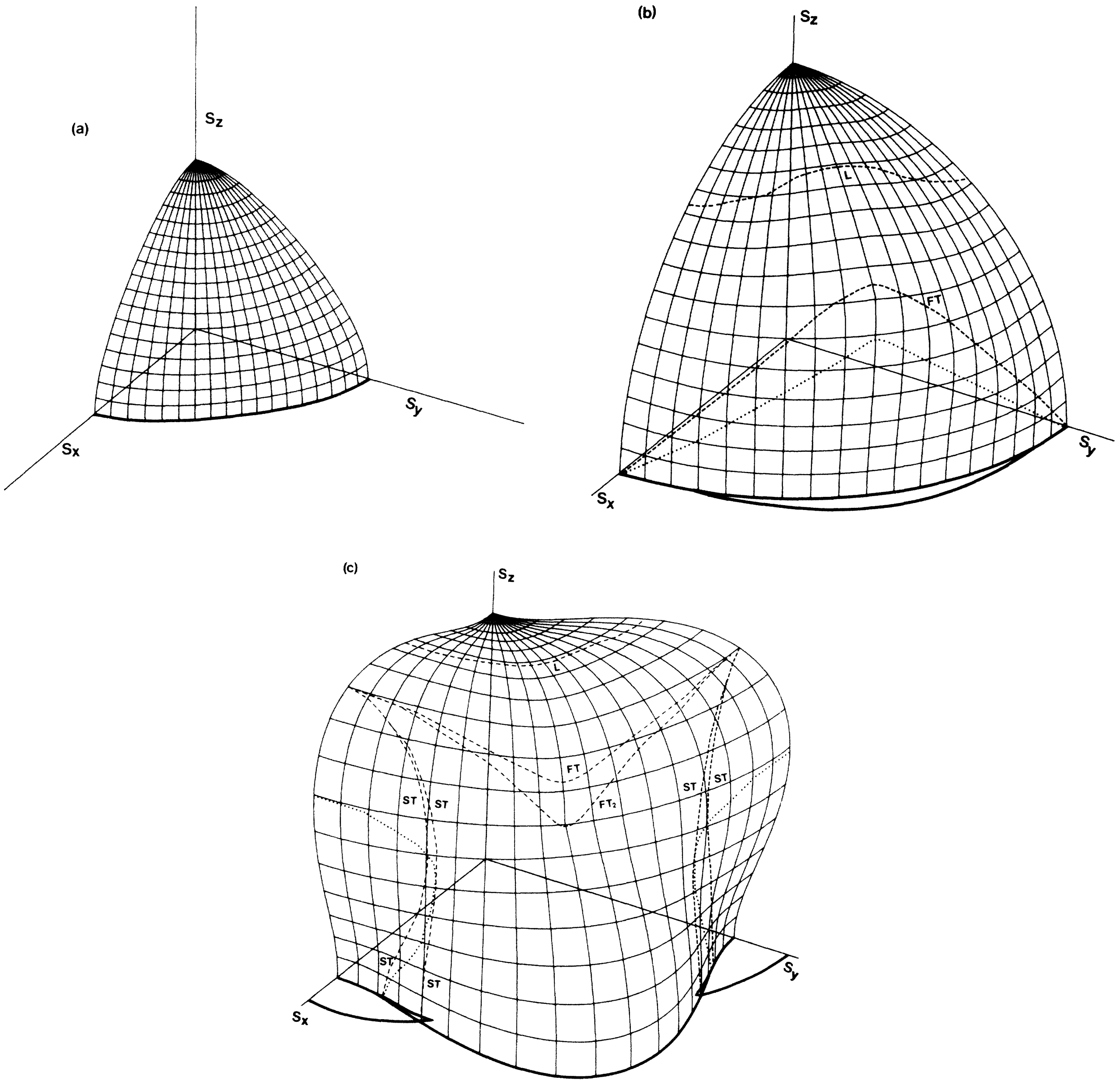

FIG. 1. The three sheets of the slowness surface of CdTe: (a) longitudinal (L), (b) fast transverse (FT), and (c) slow transverse (ST). The S_x, S_y, and S_z axes are aligned along the crystallographic cube axes. Heavy lines are the critical contours. They are the projection in the (S_x,S_y) plane of the dotted lines, which are the loci of extremal points on the slowness surface, and also of the dashed lines, which are the intersection of the **S**-space critical cones with the slowness surface. The **V**-space critical cones are composed of rays emanating normally from the slowness surface at the dashed lines.

cate the position of the associated reentrant critical cones. The second critical contour is the projection of the dotted line, where FT rays are again parallel to the (S_x,S_y) plane. Because of the mirror symmetry through this plane, there is an identical feature below the plane. Thus, on this critical contour four real solutions are replaced by two pairs of complex-conjugate solutions. The associated double-exit cone on the third sheet is labeled FT$_2$. The slow transverse (ST) sheet has large indentations, regions where both principal curvatures are negative, surrounding the cube directions. As a result, near the S_x and S_y directions there is a reentrant critical contour and also a double-exit contour. These split up and merge in a rather complex fashion at about 20° from the cube direction to form a single-exit contour. The reentrant contour gives rise to the split reentrant critical cone labeled ST. The existence of reentrant cones evidently requires that at least one principal curvature of the slowness surface be negative. A negative curvature, in turn, implies the existence of phonon-focusing caustics. For the case in point, the furrows in the FT sheet give rise to intense line caustics running between the cube directions, while the indentations in the ST sheet bring about an intense, complex, focusing structure surrounding the cube directions. These focusing structures are a prominent feature of the phonon-intensity plots for CdTe and Ge provided later in this paper.

Where complex-conjugate solutions occur, one has a positive imaginary part and represents an inhomogeneous (evanescent) wave falling off exponentially in amplitude towards the interior of the crystal. The other solution, with a negative imaginary part, represents an inhomogeneous wave showing exponential growth in the interior of the crystal, and is discarded as unphysical. There are thus always three outgoing waves $\mathbf{u}^{(i)}$, $i=1,2,3$, to consider which phase-match to any incoming bulk wave $\mathbf{u}^{(0)}$. The combined displacement field therefore has the form

$$\mathbf{u}=\mathbf{U}^{(0)}\exp[i\omega(\mathbf{S}^{(0)}\cdot\mathbf{r}-t)] + \sum_{n=1}^{3}\Gamma_n\mathbf{U}^{(n)}\exp[i\omega(\mathbf{S}^{(n)}\cdot\mathbf{r}-t)] \ . \tag{5}$$

The associated strain and stress fields are

$$\varepsilon_{pq}=\frac{1}{2}\left[\frac{\partial u_p}{\partial r_q}+\frac{\partial u_q}{\partial r_p}\right] , \tag{6}$$

and

$$\sigma_{ij}=C_{ijpq}\varepsilon_{pq} , \tag{7}$$

respectively. The weighting factors Γ_n in Eq. (5) are determined by the free-surface boundary conditions, i.e., the vanishing of the traction forces[18]

$$\sigma_{i3}(z=0)=0 \ . \tag{8}$$

This yields a set of three linear equations

$$A_{in}\Gamma_n=B_i , \tag{9}$$

where

$$A_{in}=C_{3ipq}U_p^{(n)}S_q^{(n)} \tag{10}$$

and

$$B_i=-C_{3ipq}U_p^{(0)}S_q^{(0)} , \tag{11}$$

summation over repeated subscripts being implied.

The solution to Eq. (9) takes the form

$$\Gamma_n=\frac{\tilde{A}_{nm}B_m}{|A_{pq}|} , \tag{12}$$

where $\tilde{A}_{nm}$ is the co-factor of the matrix element A_{nm}, and $|A_{pq}|$ is the boundary-condition determinant. The magnitude of the displacement field $\mathbf{u}(z=0)$ at the surface is to a large extent governed by the value of this determinant. Minima in $|A_{pq}|$ generally result in maxima in the values of Γ_n and, in turn, $|\mathbf{u}(z=0)|$, unless the factors $A_{nm}B_m$ happen to have a cancelling effect because of symmetry or for any other reason.

Figure 2 shows the variation of $|A_{pq}|$ with $|\mathbf{S}_{||}|$ for a number of different directions in the cube plane of Ge. It is interesting to compare these curves with Fig. 3, which depicts the behavior of

$$I_{\text{tot}}=\sum|\mathbf{u}(z=0)|^2 , \tag{13}$$

the summation being over incident bulk waves (1, 2, or 3) which share a common $\mathbf{S}_{||}$. Quite clearly, I_{tot} displays a number of sharp peaks or resonances, all of which coincide with minima in $|A_{pq}|$.

The vanishing of $|A_{pq}|$ in a region where only complex solutions to Eq. (2) occur is the condition for a gen-

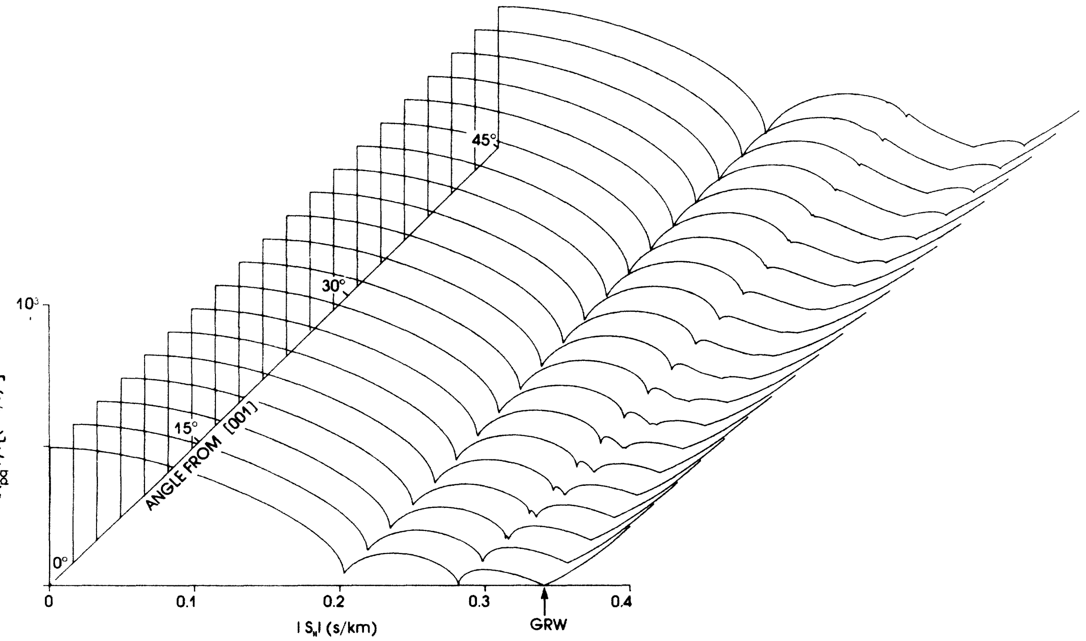

FIG. 2. Variation of the boundary-condition determinant $|A_{pq}|$ with $|\mathbf{S}|$ for a number of directions in the cube surface of Ge.

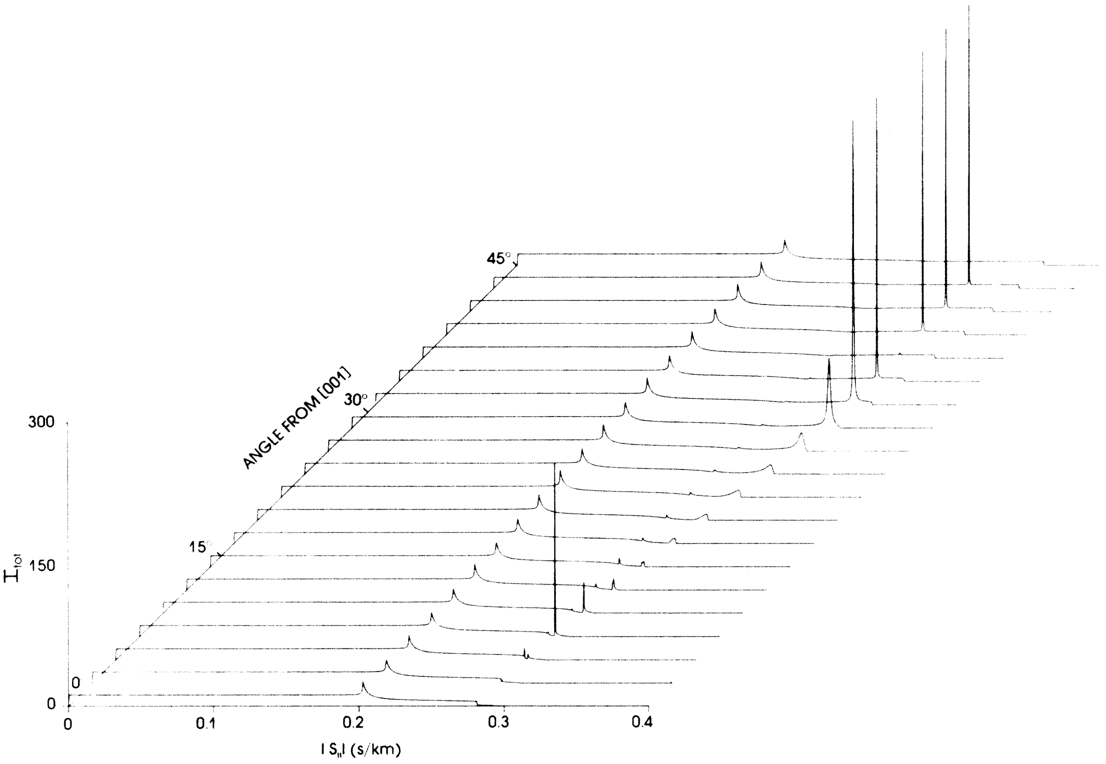

FIG. 3. Variation of I_{tot} with $\mathbf{S}_{\parallel}$ in the cube surface of Ge.

eralized Rayleigh wave (GRW). This wave consists just of three inhomogeneous partial waves and is a true surface wave in that the amplitudes of these three components fall off exponentially away from the surface. The last minimum of $|A_{pq}|$ in Fig. 2 belongs to a GRW. Lim and Farnell[9] have extended this concept by attaching the term "pseudosurface wave" to deep but nonzero minima in the boundary-condition determinant. The sharp resonances in I_{tot} can thus all be ascribed to PSW's. Energy-flux conservation normal to the surface, of course, places constraints on which of the Γ_n can become large. A large Γ_n has to belong either to an inhomogeneous wave or to a bulk wave whose ray vector is nearly parallel to the surface.

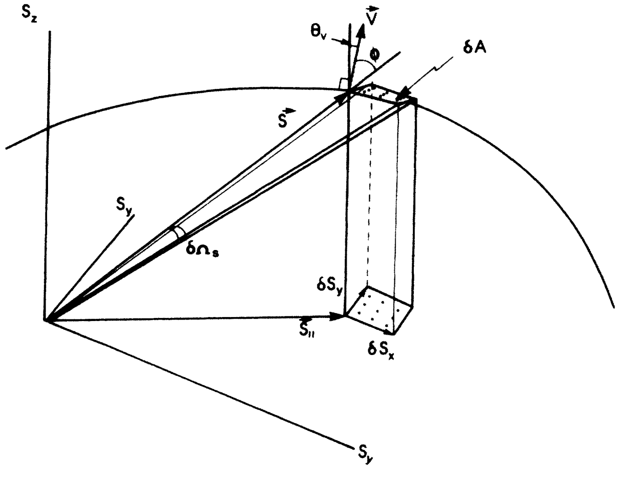

FIG. 4. Schematic diagram depicting the generation of slowness and ray vectors. Only one of the three sheets of the slowness surface is shown.

The Monte Carlo method we have used in constructing the phonon images and intensity diagrams below is explained by reference to Fig. 4. To start with, a uniform random distribution of values of $\mathbf{S}_{\parallel}$ are generated in the region enclosed by the outermost critical contour. The rectangular interval depicted would contain $N\delta S_x \delta S_y$ such $\mathbf{S}_{\parallel}$'s, where N is the areal number density. This interval is the projection in the (S_x, S_y) plane of the area element δA of the slowness surface. Each $\mathbf{S}_{\parallel}$ is the projection of an $\mathbf{S}$ contained in δA.

From inspection,

$$\delta A = \delta S_x \delta S_y / \cos\theta_V \ , \tag{14}$$

where θ_V is the angle between the ray vector $\mathbf{V}$, which is normal to the slowness surface, and the S_z direction. The solid angle subtended at the origin by δA is

$$\delta\Omega_s = \frac{\delta A \cos\phi}{S^2} = \frac{\delta S_x \delta S_y}{\cos\theta_V} \frac{\cos\phi}{S^2} \ , \tag{15}$$

where ϕ is the angle between $\mathbf{V}$ and $\mathbf{S}$. It follows that the number of $\mathbf{S}$'s per unit solid angle is

$$N_s = \frac{N\delta S_x \delta S_y}{\delta\Omega_s} = \frac{NS^2 \cos\theta_V}{\cos\phi} \ . \tag{16}$$

Making use of the well-known relation[18–20]

$$\mathbf{V}\cdot\mathbf{S}=VS\cos\phi=1\ ,\tag{17}$$

we obtain

$$N_s=NVS^3/\cos\theta_V=\frac{NV}{v^3}\cos\theta_V\ ,\tag{18}$$

where $v=1/S$ is the phase velocity. These slowness vectors $\mathbf{S}$ are evidently distributed in accordance with Lambert's Law, i.e., falling off in density as $\cos\theta_V$. Furthermore, the factor $1/v^3$ corresponds to what the Debye model yields for the heat capacity of these modes, and the factor V converts this into heat flux. Most phonon-imaging calculations in the past have ignored these factors and have simply adopted an isotropic distribution of phonon wave vectors.[13] The $\cos\theta_V$ factor has the most noticeable effect, causing polar plots of phonon intensity to fall to zero as $\theta_V\rightarrow 90°$. The factor V/v^3 accounts for the relatively small size of the L peaks in ballistic heat pulses in comparison with the T peaks. Its influence on phonon images becomes greater the more anisotropic a crystal.

The absorptivity of the surface for any mode is, on the basis of arguments presented earlier, taken to be proportional to

$$I=|\,\mathbf{u}(z=0)\,|^2\ ,\tag{19}$$

where $\mathbf{u}(z=0)$ is the displacement caused in the free surface by that normalized mode.

The image-construction process then consists of determining the incoming rays for each value of $\mathbf{S}_{\parallel}$ in the distribution, giving these a weighting proportional to I, and then sorting these rays in direction to form a polar density plot for the phonon intensity. In the case of Figs. 5 and 6, the phonon intensity has been projected onto the appropriate crystallographic planes in order to obtain a spatial density diagram that can be directly compared with published experimental images.

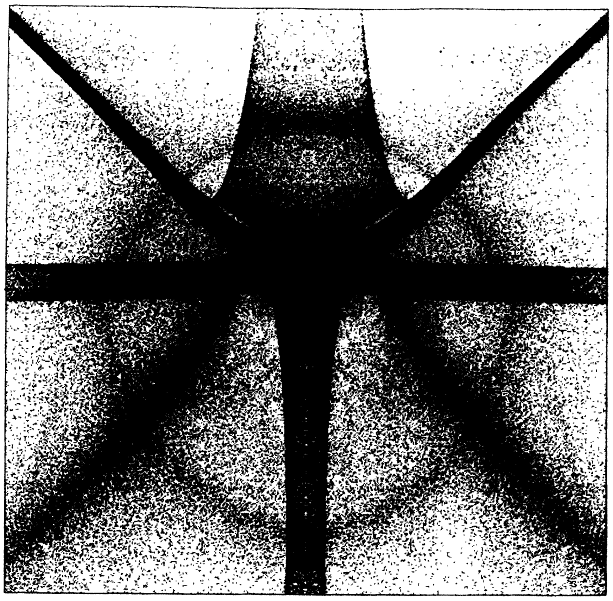

FIG. 5. Calculated phonon image for sapphire with ($\theta=58°$, $\phi=30°$) surface orientation. The horizontal and vertical half-angles of view are ±32°. Only the ST and FT phonon fluxes are displayed. Phonon intensity is represented by the darkness of the greyscale, which comes from the density of printing points. The elastic constants for the calculation are taken from Ref. 25.

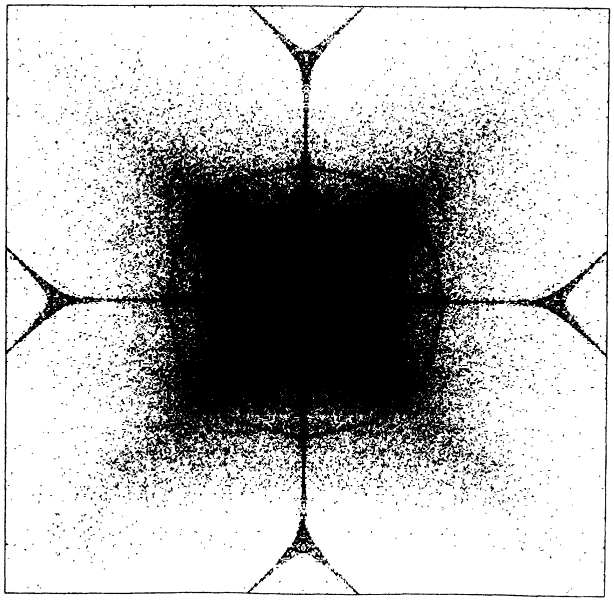

FIG. 6. Calculated phonon image for diamond with (100) surface orientation. Horizontal and vertical half-angles of view are ±60°. The [111] direction is in the center of the threefold structure near the top center of the image. The elastic constants for the calculation are taken from Ref. 26.

One should bear in mind that surface-directivity effects may arise at heater and detector interfaces and are multiplicative. When these surfaces are not parallel, two independent sets of surface-derived structure can be present in a phonon image.[16]

III. COMPARISON WITH PUBLISHED EXPERIMENTAL DATA

Figure 5 shows a calculated Monte Carlo image for sapphire, the projection surface being parallel to the ($\theta=58°$, $\phi=30°$) crystallographic plane (θ and ϕ here are the spherical polar coordinates of the surface normal). In this and all subsequent images and intensity plots only the ST and FT phonon flux is displayed. The L phonons (or more precisely the inner-sheet phonons[24]) do not exhibit any sharp features either as a result of phonon focusing or through PSW resonances. Experimentally, the L phonons are in any case often eliminated by suitable time gating of the detector signal. The emissivity I for this image is almost constant, except in the vicinity of the roughly circular halo where, for the ST branch, it rises considerably above the background value. All the other structures in this image are bulk-phonon-focusing singularities. This calculated image is in very good agreement with experimental images reported by Koos *et al.*[14] and Every *et al.*[15] for sapphire with this orientation. The ST phonons comprising the halo are all located close to the critical cone for mode conversion from ST to L. This enhancement of *I*, called critical-cone channeling,[15] is brought about by a PSW of L character in the surface. There is no significant FT→L channeling because of the fact that the FT phonons that would participate in channeling all have polarization vectors which are very nearly

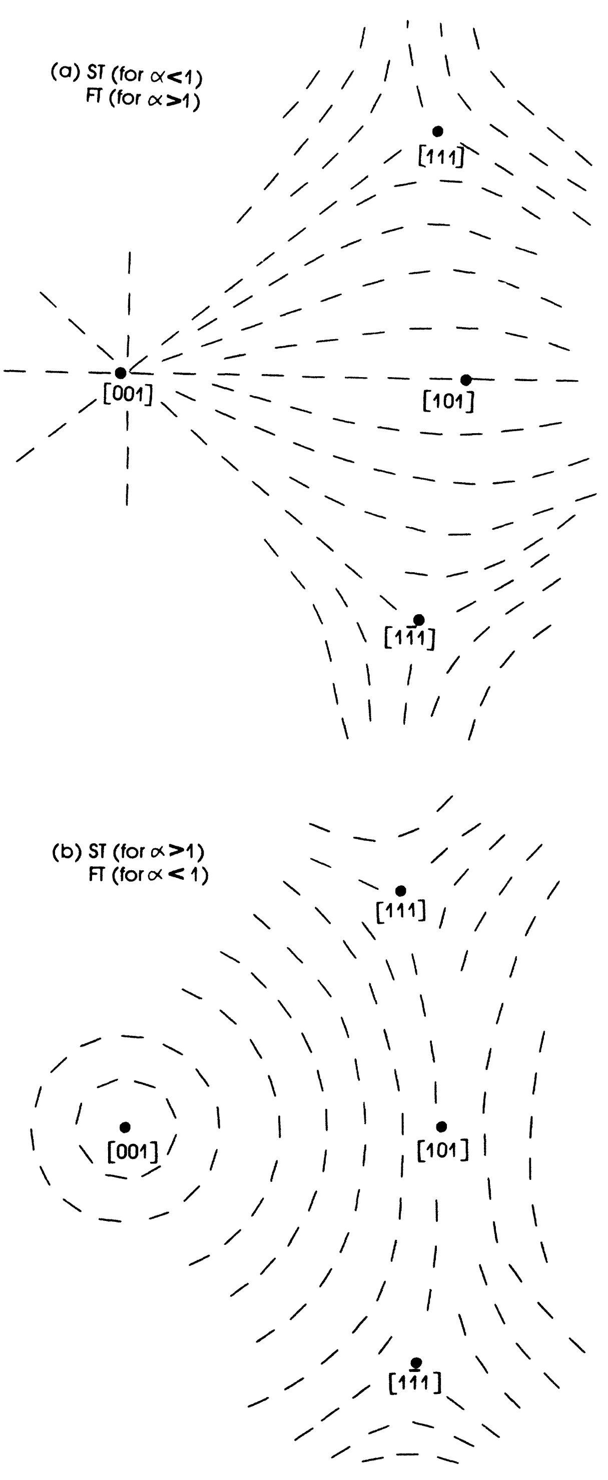

FIG. 7. Polarization fields for the FT and ST branches for cubic crystals of moderate anisotropy. There are singularities in the fields in the [001] and [111] directions, where the two branches are degenerate.

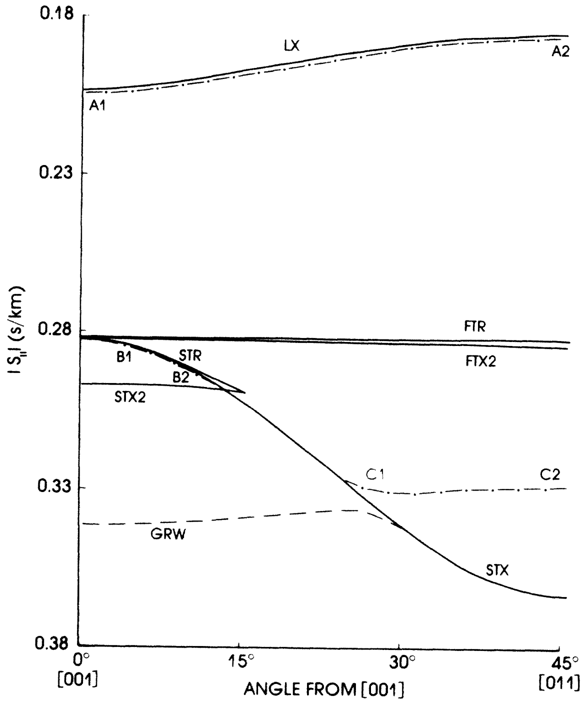

FIG. 8. Critical contours (solid lines), the more prominent PSW resonances (dashed-dotted lines), and generalized Rayleigh wave (dashed line) for the (100) surface of Ge. Critical contours are identified with regard to branch (L, FT, or ST), whether exit (X) or reentrant (R) and if double (2). Points labeled *A* 1, *A* 2, *B* 1, etc. on the PSW resonances are mapped onto similarly labeled points in the phonon-intensity diagram in Fig. 9.

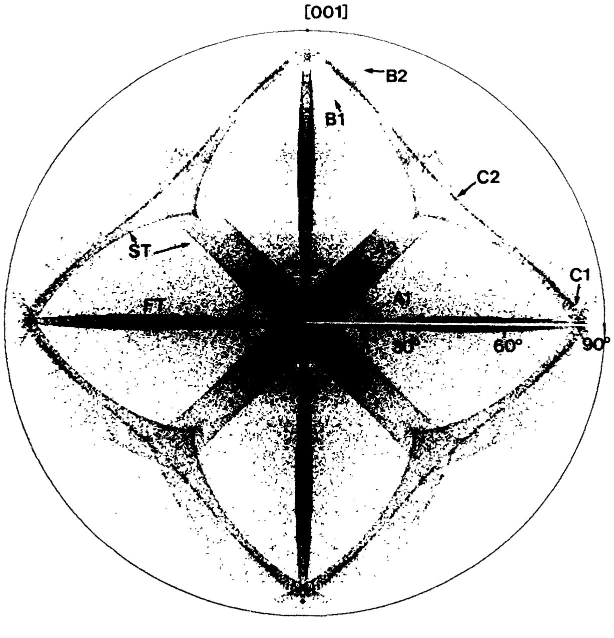

FIG. 9. Polar diagram of ST and FT phonon intensity for the (100) surface of Ge. Bulk-phonon-focusing caustics are identified by branch (ST or FT). Points labeled *A* 1, *A* 2, *B* 1, etc. on the PSW structures are mapped from similarly labeled points in Fig. 8.

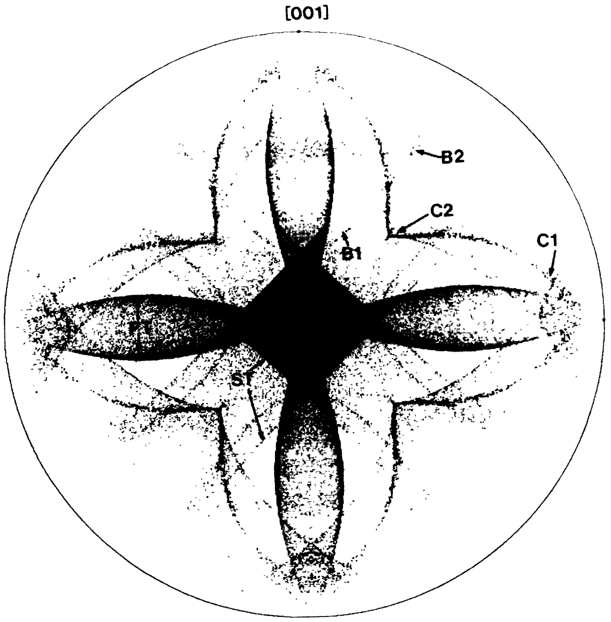

FIG. 10. Polar phonon-intensity diagram for the (100) surface of CdTe.

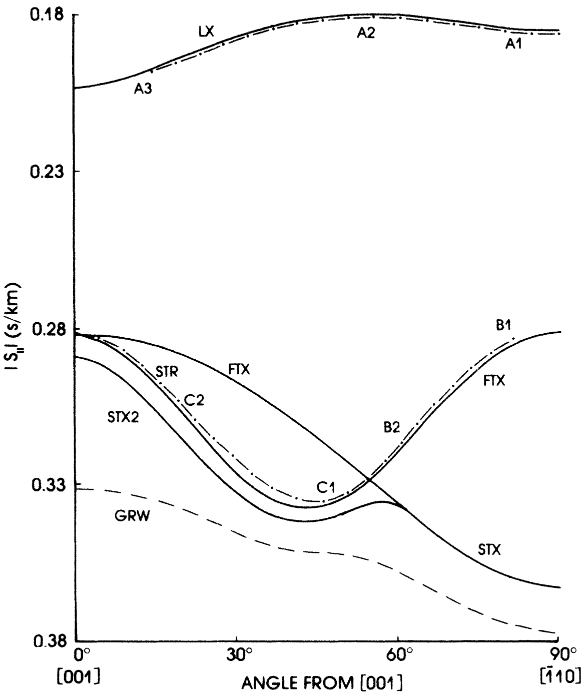

FIG. 12. Critical contours, prominent PSW resonances, and Rayleigh wave for the (110) surface of Ge.

perpendicular to their sagittal planes. They are, consequently, almost totally uncoupled at the surface from the other two branches, which are polarized in or close to their sagittal planes.

Concerning the actual computations, approximately 700 000 values of $\mathbf{S}_{\|}$ were used in the construction of the image in Fig. 5. This includes a factor of 2 gained by exploiting the mirror symmetry through the center line of the image. The computations were done on an IBM 3083 mainframe computer and took about 60 min of CPU time. Images and phonon-intensity plots with a higher degree of symmetry took proportionately less time. Much of this time was taken up in solving the sextic equation (2). In cases where the crystal surface is a mirror plane, this equation reduces to a bicubic and the overall computational time was reduced further by about a factor of 2. The weighted and sorted ray vectors were stored in a 512×512 array which was subsequently downloaded to a

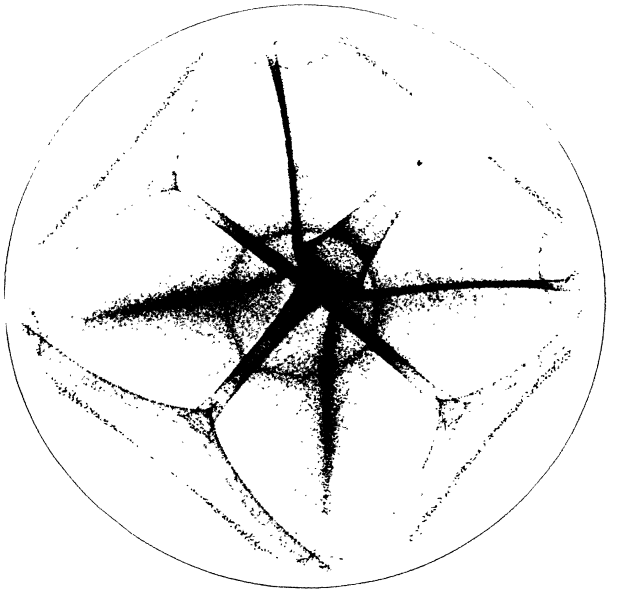

FIG. 11. Polar phonon-intensity diagram for the (58°,30°) surface of sapphire (rotated by 45° with respect to the orientation in Fig. 5).

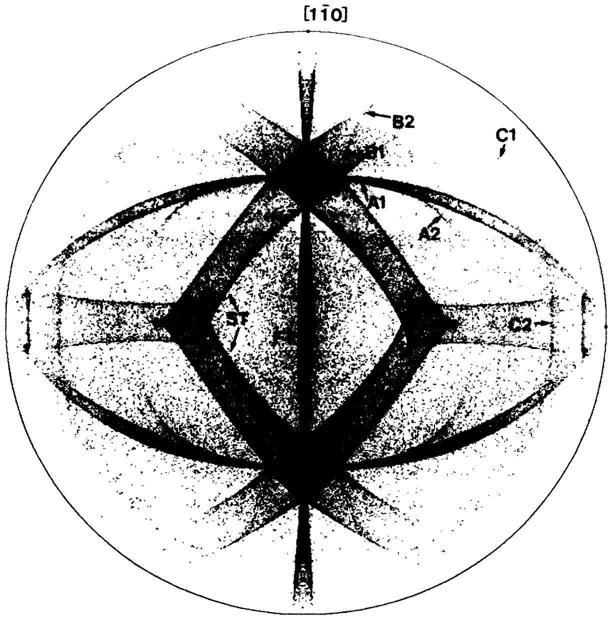

FIG. 13. Polar phonon-intensity diagram for Ge(110).

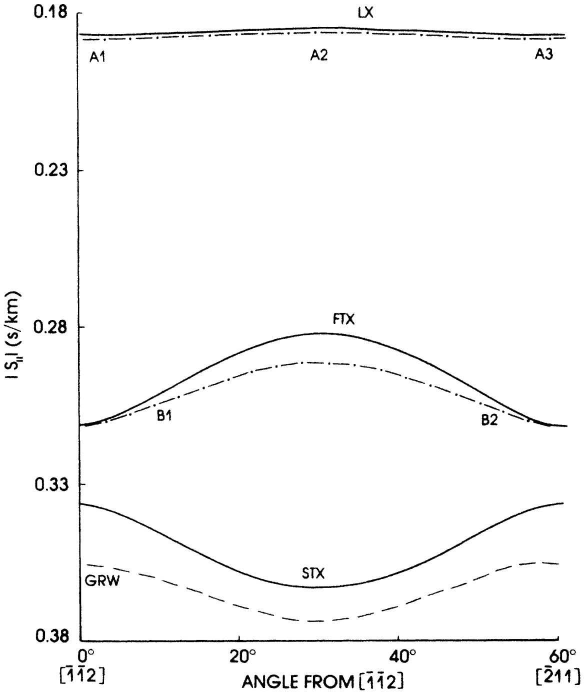

FIG. 14. Critical contours, prominent PSW resonances, and Rayleigh wave for Ge(111).

Hewlett Packard (HP) 9836 minicomputer and printed on an HP 2934A graphics printer. The dot density in the image is proportional to the phonon intensity.

Figure 6 shows a calculated image for the (100) surface of diamond. As in the case of sapphire, there is a prominent circular halo arising from ST→L critical-cone channeling. This image is in very good agreement with the experimental images reported for diamond by Hurley *et al.*[16] In comparison with that of sapphire, the diamond ST halo is extremely sharp. As before, there is no visible FT channeling.

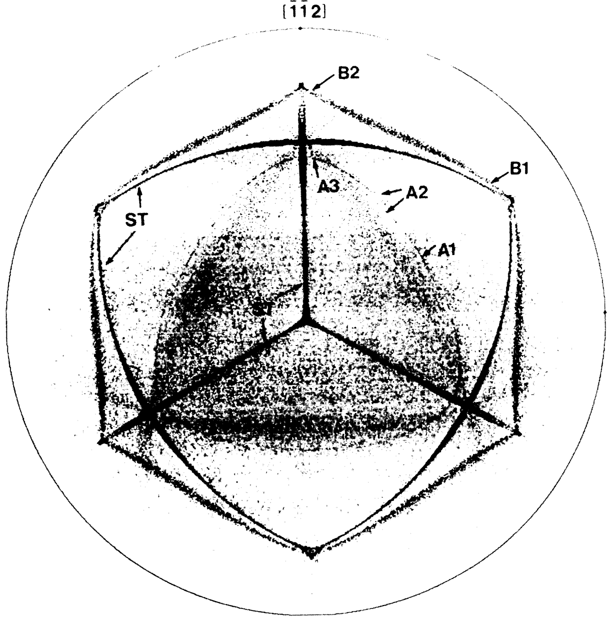

FIG. 16. Polar phonon-intensity diagram for diamond (111).

To sum up then, our model is able to account very well for the channeling (as well as focusing) structures in published experimental images without recourse to the use of any free parameters. This gives us some confidence in the basic soundness of the model. In the next section we ap-

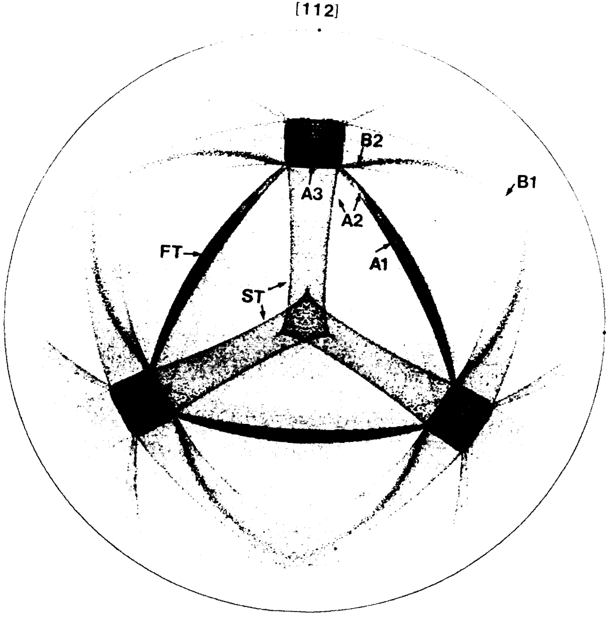

FIG. 15. Polar phonon-intensity diagram for Ge(111).

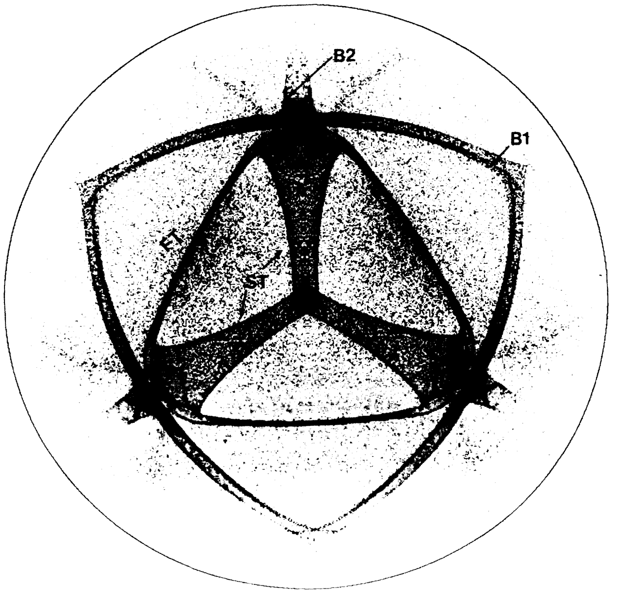

FIG. 17. Polar phonon-intensity diagram for the sapphire *XY* surface.

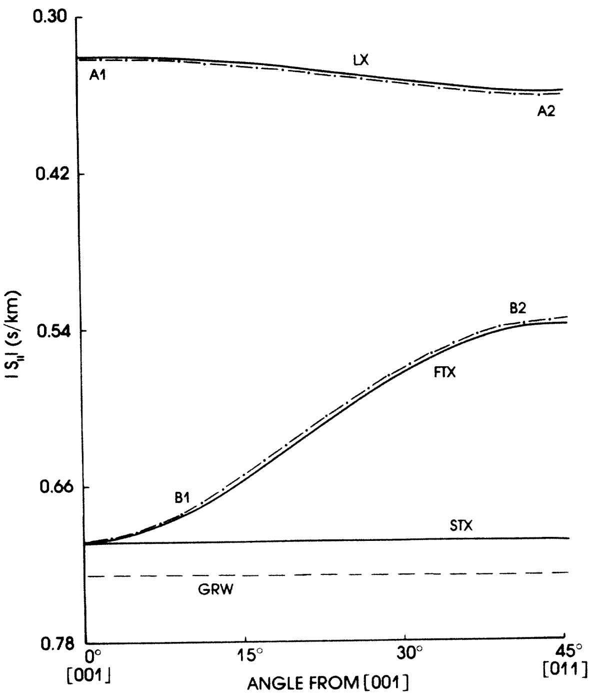

FIG. 18. Critical contours, PSW resonances, and Rayleigh wave for CsCl (100).

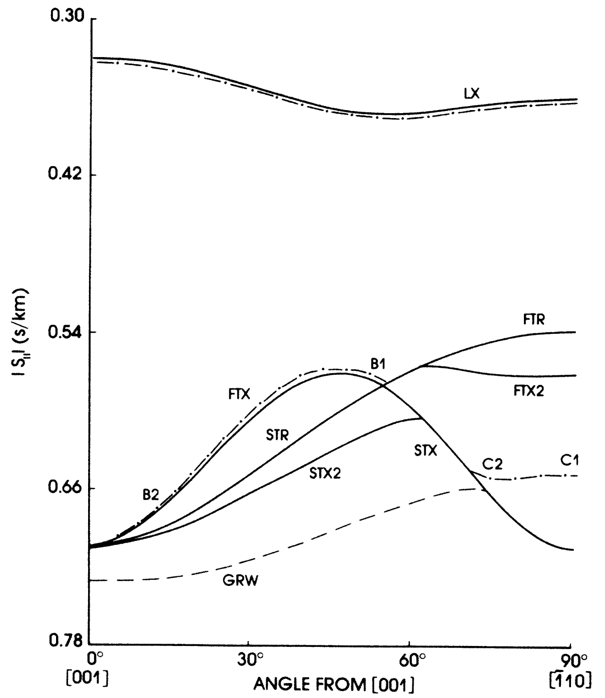

FIG. 20. Critical contours, prominent PSW resonances, and Rayleigh wave for CsCl(110).

ply the model to a range of different materials and surfaces.

IV. PREDICTIONS OF THE MODEL

The directional dependence of phonon intensity in our model is determined uniquely by the ratio of the elastic constants for a crystal and its surface orientation. In the case of cubic crystals, it is to some extent possible to distinguish between the effect of anisotropy, as characterized by the parameter $\alpha=(C_{11}-C_{12})/2C_{44}$ and the L to T velocity ratio, as characterized by the parameter $\beta=(C_{11}+C_{12})/2C_{44}$. In some cases, as we will show, the phonon-intensity patterns of crystals of lower symmetry bear a close resemblance to those of cubic crystals.

A factor which, as mentioned earlier, plays an important role in distributing the resonant phonon intensity from longitudinal PSW's between the ST and FT

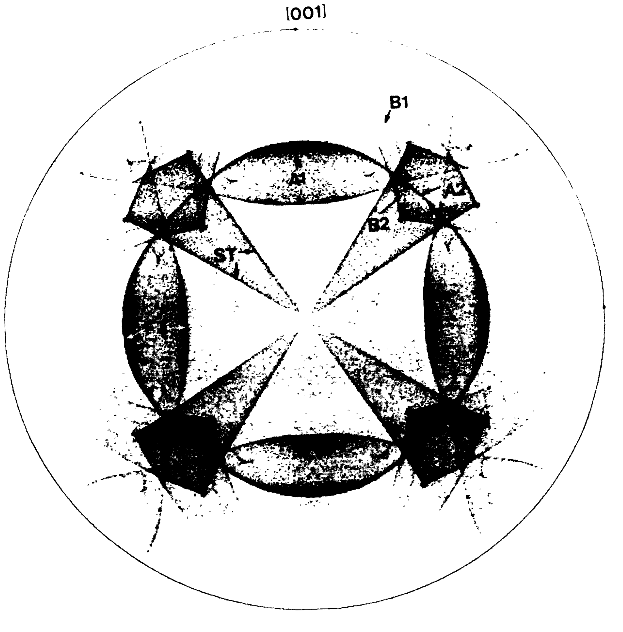

FIG. 19. Polar phonon-intensity diagram for CsCl(100).

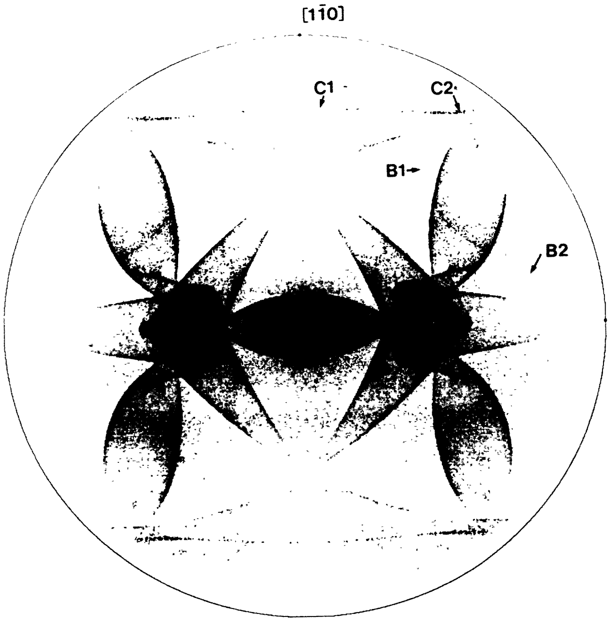

FIG. 21. Polar phonon-intensity diagram for CsCl(110).

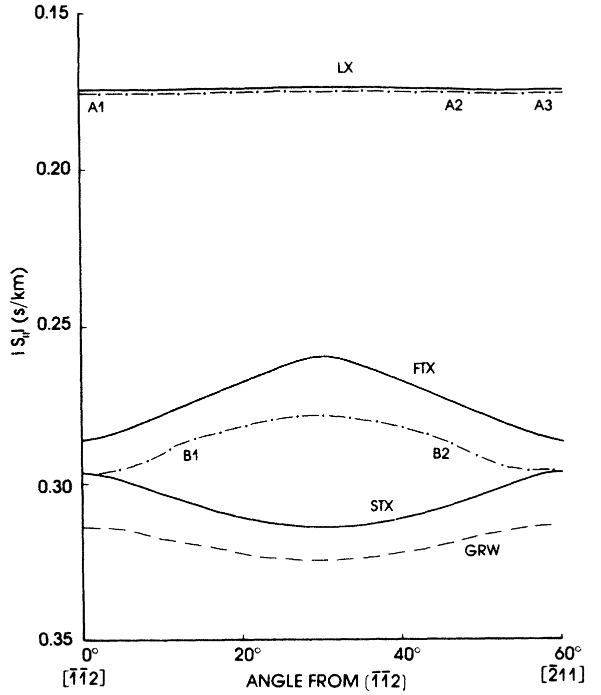

FIG. 22. Critical contours, PSW resonances, and Rayleigh wave for NaF(111).

branches, is the polarization field for these branches. Providing the anisotropy is not too large, the polarization field for the L branch is nearly normal to the unit sphere, while the fields for the ST and FT branches lie almost on the unit sphere and form the patterns shown in Fig. 7. A ST wave approaching a (001) surface at not too large an angle to the normal is, for $\alpha < 1$, polarized in the sagittal plane, and therefore can participate in mode conversion to L. A FT wave, on the other hand, is polarized normal to the sagittal plane and is not able to mode-convert. As a result, ST→L critical-cone channeling is far more pronounced than FT→L channeling. For $\alpha < 1$ the converse holds. It is the FT phonons which are in this case polarized in the sagittal plane and strongly channeled.

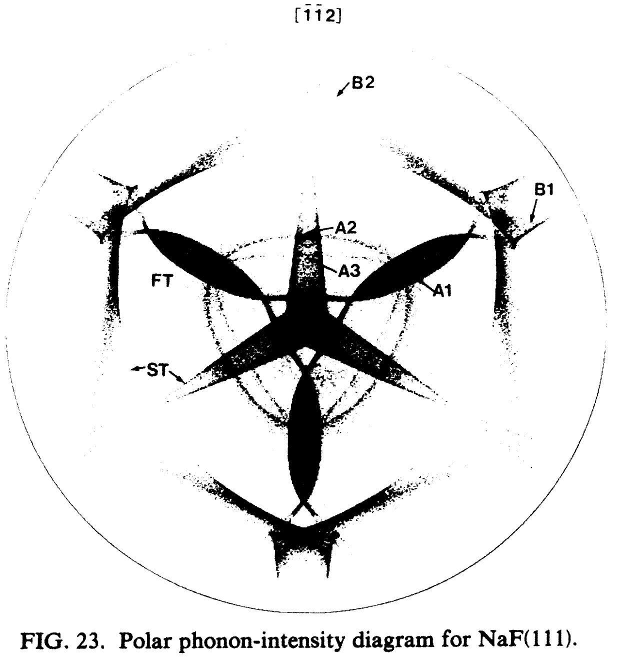

FIG. 23. Polar phonon-intensity diagram for NaF(111).

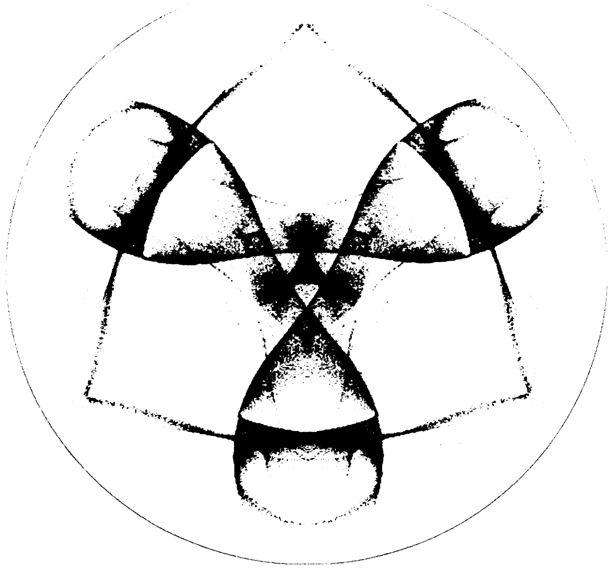

FIG. 24. Polar phonon-intensity diagram for the quartz *XY* surface. The elastic constants for the calculation are taken from Ref. 31.

For a (111) surface the ST polarization changes from sagittal to normal to sagittal three times in a circuit around the normal. When the ST polarization is sagittal, the FT polarization is normal, and vice versa. This causes the channeling to swing between the ST and FT branches, going through three complete cycles in 360°.

For a (101) surface the situation is slightly more complicated. On a cone of small angle the swinging of the channeling between ST and FT goes through two complete cycles in 360°. When the cone angle exceeds 35.26°, the cone encompasses the [111] and [$1\bar{1}1$] directions and now the swinging of the channeling between ST and FT goes through four cycles in 360°. An added complication is that modes near the $\langle 111 \rangle$ conical points have their rays spread out over a large solid angle, making the channeling structures fainter and more difficult to unravel.

The effect of β on ST→L and FT→L critical-cone channeling is twofold. As β increases, the L sheet of the slowness surface becomes smaller in comparison with the T sheets. As a result the critical-cone angle also becomes smaller. The width of the T→L channeling resonance also depends on β, being zero when $\beta = 1$ and increasing as β departs from 1 in either direction. The reason for this[16] is that as $\beta \rightarrow 1$ Poisson's ratio tends to zero, and the longitudinal PSW giving rise to the channeling evolves into a surface-skimming bulk L wave satisfying the free-surface boundary conditions on its own.

A. Crystals with $\alpha < 1$

Figure 8 shows the location of critical contours, PSW resonances, and the Rayleigh wave for the (100) surface of

GE ($\alpha=0.60$, $\beta=1.32$). The way in which these are arranged is common to crystals of moderately large deviation of anisotropy below 1. Figure 9 is a polar diagram of the phonon intensity for (100)-oriented Ge. The pattern formed by the ST and FT bulk-phonon-focusing caustics is well known from experimental and theoretical studies by a number of authors.[27–30] In addition, there are several PSW structures in this plot that should, under favorable conditions, be observable. There is strong channeling of ST phonons ($A1$-$A2$) over the entire ST→L exit cone, but no significant FT channeling. Because of the indentation of the ST sheet of the slowness surface around the [100] direction, the average cone angle for these channeled rays is fairly small, ~20°. This same indentation around the other ⟨100⟩ directions brings about the rather faint ST→ST reentrant critical-cone-channeling structure $B1$-$B2$. Channeling associated with the FT reentrant and exit contours is barely perceptible.

The most prominent resonance structure, $C1$-$C2$, is due to a PSW that has been the subject of considerable interest[8–10] and that has been experimentally observed in a number of different crystals.[1,3,5] The sagittal plane containing the [011] direction is a mirror plane, as is the (100) plane of the crystal surface. The FT and L waves, which for large $|\mathbf{S}_{\parallel}|$ are polarized in this sagittal plane, become decoupled from the ST wave, which is polarized normal to this plane. The outcome is that a true sagittaly polarized surface wave exists at $C2$. Even though it is immersed in a continuum of ST bulk waves, it does not communicate with them. Departing form the [011] direction, this wave acquires a small ST bulk component and becomes a resonance within the continuum. Near $C2$ this resonance is extremely narrow, becoming progressively broader toward $C1$. There is a region in the middle of this range where the resonance becomes relatively faint.

Figure 10 is a phonon-intensity diagram for the (100) surface of CdTe ($\alpha=0.41$, $\beta=2.24$). Interestingly, because of the high degree of anisotropy, the [100] indentation in the ST sheet is so large that the ST→L critical cone of rays is inverted through the [100] axis, so that mode conversion of a critical ST incombining wave results in a L wave traveling *backwards* along the surface. The large deviation of β from 1 causes the channeling structure to be fairly broad. Also, because this structure is confined to the intense focusing square at the center of the image, it is not easy to discern. The ST reentrant cone structure $B1$-$B2$ is larger and more intense than for Ge, and the PSW structure $C1$-$C2$ is also more pronounced.

In the case of diamond ($\alpha=0.82$, $\beta=1.04$) both α and β are closer to 1 than in the case of Ge. As a result, as Fig. 6, shows, the ST→L channeling structure is extremely narrow and almost circular in shape. The distortion of the slowness surface is so slight that the ⟨100⟩ indentations in the ST sheet and the FT furrows and their associated reentrant cones do not exist. Also, the bulge of the ST sheet near the [011] direction is too slight to "bring it into collision" with the Rayleigh wave, and, consequently, there is no PSW $C1$-$C2$.

Figure 11 is a phonon-intensity diagram for the (58°,30°) surface of sapphire. It is rotated by 45° with respect to Fig. 5. As can be seen, it bears a striking resemblance to the Ge(100) phonon-intensity diagram, particularly with regard to the PSW structure $C1$-$C2$ and its relation to the focusing structures.

The PSW structures for the Ge(110) surface are all rather faint. Figure 12 shows the location of critical contours and PSW resonances, and Fig. 13 is the polar phonon-intensity diagram for this surface. The L exit-cone channeling is predominantly FT between $A1$ and $A2$ and ST between $A2$ and $A3$, where it is highly dispersed in direction by the effects of conical refraction and barely visible. There is a faint ST→FT critical-cone-channeling structure $B1$-$B2$ and somewhat more visible ST reentrant channeling $C1$-$C2$.

Figure 14 shows the critical contours and PSW resonances for the (111) surface of Ge, and Fig. 15 is the phonon-intensity diagram for this surface. There are no reentrant contours, and because the (111) surface is not a crystal-symmetry plane, the slowness surface does not intersect it along the exit lines, but at somewhat smaller values of $|\mathbf{S}_{\parallel}|$. Channeling for the L exit contour alternates between ST and FT. These channeling structures are drawn toward strong focusing regions and become partially obscured in the process. The very intense PSW structure $B1$-$B2$ occurs a little distance from the ST→FT critical cone. At the two extremes, beyond $B1$ and $B2$, this PSW degenerates into a surface-skimming bulk FT wave[9] polarized normal to the sagittal plane, which is a crystal-symmetry plane. This PSW has been observed in silicon using the acoustical wedge technique by Pratt and Lim.[3]

Figure 16 is a phonon-intensity plot for the (111) surface of diamond. The ST→L channeling structure $A1$-$A2$ and FT→L channeling structure $A2$-$A3$ are sharp and faint but visible. By comparison, the PSW structure $B1$-$B2$ is extremely intense.

Figure 17 is a phonon-intensity diagram for the sapphire *XY* surface. It bears a striking resemblance to the intensity pattern for Ge(111), with regard to focusing as well as PSW structures. The ST→L channeling structure *A* matches up very well with corresponding features in the experimental images of Every *et al.*[15] The analogue of the $B1$-$B2$ PSW structures is very intense, as in the cases of Ge and diamond.

B. Crystals with $\alpha > 1$

Figure 18 shows the critical contours and PSW resonances for the (100) surface of CsCl ($\alpha=1.71$, $\beta=2.83$), and Fig. 19 is the phonon-intensity diagram for that surface. The various features seen in these two figures are common to crystals of moderately large anisotropy α (>1). There is strong FT→L critical-cone channeling, which produces the intense circular structure $A1$-$A2$. This channeling is drawn toward nearby FT focusing caustics and in some places is not easily resolved from them. There is fairly sharp channeling structure $B1$-$B2$ at the ST→FT critical cone.

Figure 20 shows the critical contours and PSW resonances for the CsCl (110) surface, and Fig. 21 is the phonon-intensity diagram for that surface. The ST→L and FT→L critical-cone-channeling structures lie very close to focusing caustics and are not easily resolved. There is a faint channeling structure $B1$-$B2$ associated with the FT exit contour. The most prominent PSW structure is $C1$-$C2$. At $C1$ it evolves into a true surface wave polarized in the sagittal plane, which is a crystal-symmetry plane.[9,10]

Figure 22 shows the critical contours and PSW resonances for the NaF (111) surface, and Fig. 23 is the phonon-intensity diagram for that surface. There are well-defined FT$\rightarrow$L and ST$\rightarrow$L critical-cone-channeling structures, $A1$-$A3$ and $A1$-$A2$, respectively. In the region of $A2,A3$, polarization favors FT channeling, while bulk focusing strongly enhances the ST intensity. Near $A1$ it is the other way around. As a result, the alternation between FT and ST channeling is not readily apparent. Just a small distance beyond the ST$\rightarrow$FT exit cone there is the broad, fairly intense PSW structure $B1$-$B2$. At the two extremes near $B1$ and $B2$ it degenerates into a surface-skimming bulk ST wave.[9]

Finally, Fig. 24 shows the phonon-intensity diagram for the XY surface of quartz. There is a fair degree of similarity between this diagram and the NaF(111) diagram. The analogue of the PSW structure $B1$-$B2$ is intense and well defined.

V. DISCUSSION

Free-crystal surfaces are able to support a wealth of different pseudosurface waves. These PSW's differ from true surface waves in that they contain a small bulk-wave component through which they can be excited and into which they can decay. We have developed a simple parameter-free model for calculating the effects of PSW's on phonon images. Our model treats the coupling between the crystal and metal overlayers, used for phonon generation and detection, as an isotropic dissipative mechanism, and it is applicable to situations where the metal overlays are of low acoustic impedance or are weakly bonded to the crystal substrate. In the limit of weak loading, the directional dependence of the phonon transmission across the interface is largely dictated by the properties of the crystal and is relatively insensitive to the precise nature of the overlayer or form of the boundary conditions. All the phonon-intensity plots we have calculated display well-defined structures due to PSW's. In some case these resonant structures become exceedingly sharp near limiting directions in which the PSW evolves into a true surface wave immersed in a bulk-wave continuum.

Our calculated images for sapphire and diamond are in very good agreement with published experimental images for these crystals. Because of the high acoustic impedances and velocities of these two materials, the conditions of our model are relatively easily met. For crystals having lower acoustic impedances and velocities, deliberate action will, in general, be required to achieve the weak loading condition. Increased loading of the crystal surface leads to the softening and eventual suppression of the PSW structures.

Another important factor is the roughness of the crystal surface. Roughness on the scale of the dominant thermal phonon wavelength or greater has the effect of smearing out the surface-directivity effects described here. For a given heat-pulse temperature, therefore, preserving PSW structures in low-Debye-temperature crystals requires a higher degree of surface smoothness than in "harder" crystals such as diamond or sapphire.

In conclusion, phonon imaging provides a useful means of studying the rich variety of resonant vibrations that occur in crystal surfaces. Its advantage over other methods for investigating PSW's is that a single image is able to provide a complete picture of all the PSW's in a given surface, and also convey an impression of how these resonances vary in intensity and width with direction. The existence of these PSW structures enhances the potential value of this technique as a sensitive tool for probing crystal surfaces and interfaces.

ACKNOWLEDGMENTS

The author would like to thank Professor M. J. R. Hoch for access to his computing facilities. He has benefited greatly in the formative period of some of the ideas presented here from discussions with Professor J. P. Wolfe.

---

[1] F. R. Rollins, T. C. Lim, and G. W. Farnell, App. Phys. Lett. **12**, 236 (1968).

[2] F. R. Rollins, J. Acoust. Soc. Am. **44**, 431 (1968).

[3] R. G. Pratt and T. C. Lim, Appl. Phys. Lett. **15**, 403 (1969).

[4] H. Engan, K. A. Ingebrigtsen, and A. Tonning, App. Phys. Lett. **10**, 311 (1967).

[5] J. R. Sandercock, Solid State Commun. **26**, 547 (1978).

[6] F. W. de Wette, Comments Solid State Phys. **11**, 89 (1984).

[7] G. Benedek, Physica **127B**, 59 (1984).

[8] V. R. Velasco and F. Garcia Moliner, J. Phys. C **13**, 2237 (1980).

[9] T. C. Lim and G. W. Farnell, J. Acoust. Soc. Am. **45**, 845 (1969).

[10] G. W. Farnell, in *Physical Acoustics*, edited by W. P. Mason and R. N. Thurston (Academic, New York, 1970), Vol. 6, p. 109.

[11] R. E. Camley and A. A. Maradudin, Phys. Rev. B **27**, 1959 (1983).

[12] V. I. Alshits and J. Lothe, Wave Motion **3**, 297 (1981).

[13] For a recent review on phonon imaging, see G. A. Northrop and J. P. Wolfe, in *Nonequilibrium Phonon Dynamics*, edited by W. E. Bron (Plenum, New York, 1985), p. 165.

[14] G. L. Koos, A. G. Every, G. A. Northrop, and J. P. Wolfe, Phys. Rev. Lett. **51**, 276 (1983).

[15] A. G. Every, G. L. Koos, and J. P. Wolfe, Phys. Rev. B **29**, 2190 (1984).

[16] D. C. Hurley, A. G. Every, and J. P. Wolfe, J. Phys. C **17**, 3157 (1984).

[17] F. Rösch and O. Weis, Z. Phys. B **27**, 33 (1977).

[18] B. A. Auld, *Acoustic Fields and Waves in Solids* (Wiley, New York, 1973).

[19] M. J. P. Musgrave, *Crystal Acoustics* (Holden-Day, San Fran-

cisco, 1970).

[20] F. I. Fedorov, *Theory of Elastic Waves in Crystals* (Plenum, New York, 1968).

[21] E. G. Henneke, J. Acoust. Soc. Am. **51**, 210 (1972).

[22] R. F. S. Hearmon, in *Landolt-Börnstein: Numerical Data and Functional Relationships in Science and Technology, New Series,* edited by K.-H. Hellwege (Springer, Berlin, 1984), Group III, Vol. 18, pp. 1–154.

[23] This follows from the fact that the equation of the slowness surface is of degree 6. See G. F. D. Duff, Philos. Trans. R. Soc. London **252**, 249 (1960).

[24] A. G. Every and A. J. Stoddart, Phys. Rev. B **32**, 1319 (1985).

[25] B. T. Bernstein, J. Appl. Phys. **34**, 169 (1963).

[26] M. H. Grimsditch and A. K. Ramdas, Phys. Rev. B **11**, 3139 (1975).

[27] G. A. Northrop and J. P. Wolfe, Phys. Rev. B **22**, 6196 (1980).

[28] A. G. Every, Phys. Rev. B **24**, 3456 (1981).

[29] J. C. Hensel, R. C. Dynes, F. C. Unterwald, and A. L. Simons, J. Phys. (Paris) Colloq. **42**, C6-212 (1981).

[30] W. Metzger, R. Eichele, H. Seifert, and R. P. Huebener, in *Phonon Scattering in Condensed Matter,* edited by W. Eisenmenger, K. Lassmann, and S. Döttinger (Springer, Berlin, 1984), p. 72.

[31] R. Bechmann, Phys. Rev. **110**, 1060 (1958).

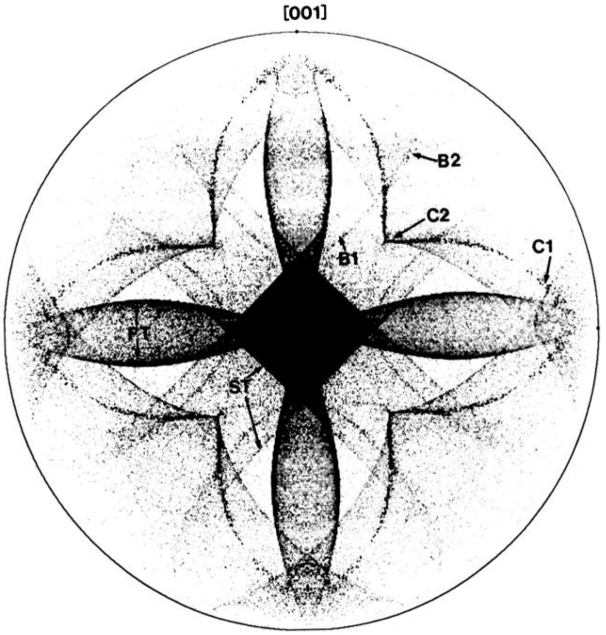

FIG. 10. Polar phonon-intensity diagram for the (100) surface of CdTe.

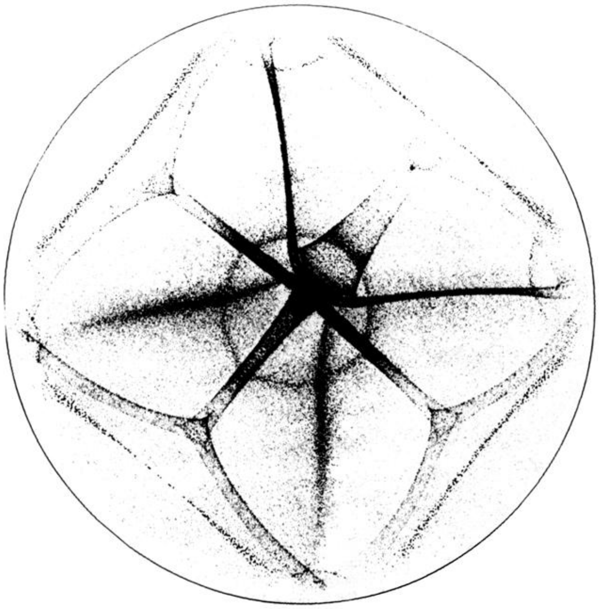

FIG. 11. Polar phonon-intensity diagram for the (58°,30°) surface of sapphire (rotated by 45° with respect to the orientation in Fig. 5).

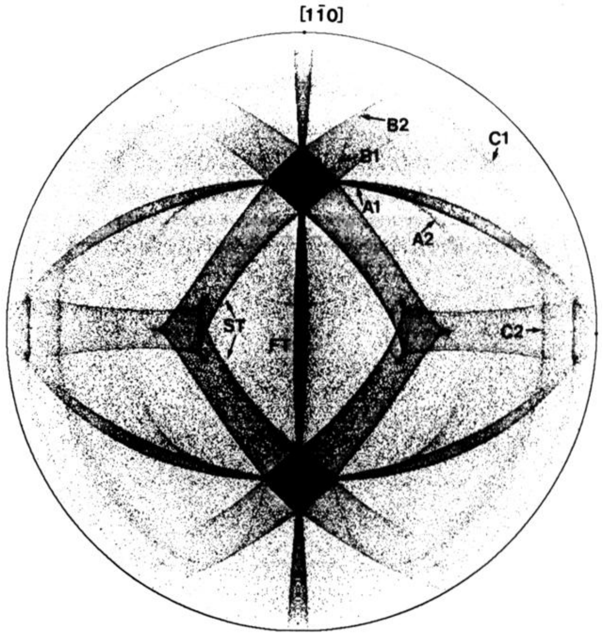
[1$\bar{1}$0]
B2
C1
B1
A1
A2
ST
FT
C2

FIG. 13. Polar phonon-intensity diagram for Ge(110).

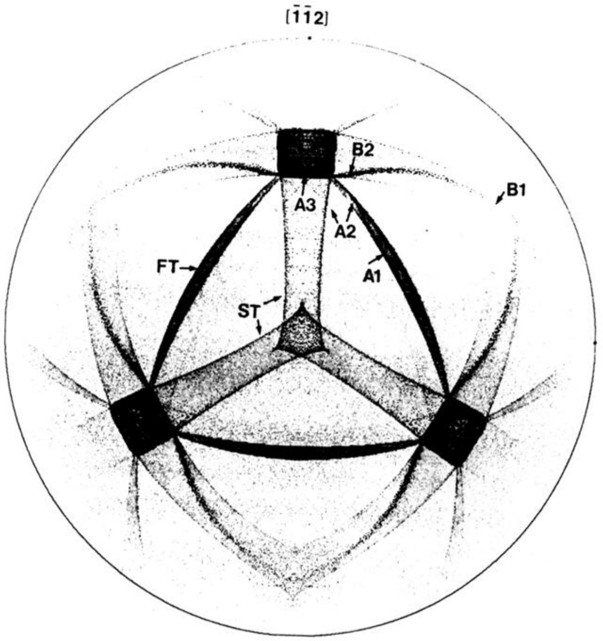
[$\bar{1}\bar{1}$2]
B2
B1
A3
A2
A1
FT
ST

FIG. 15. Polar phonon-intensity diagram for Ge(111).

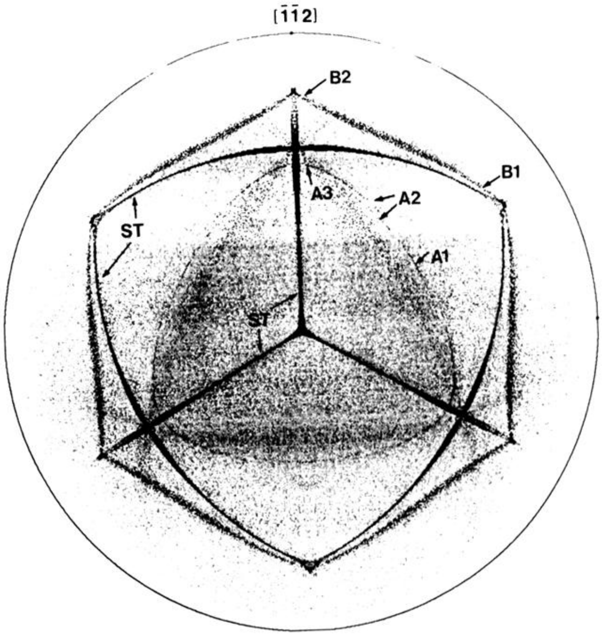
[$\bar{1}\bar{1}2$]
B2
B1
A3
A2
A1
ST
ST

FIG. 16. Polar phonon-intensity diagram for diamond (111).

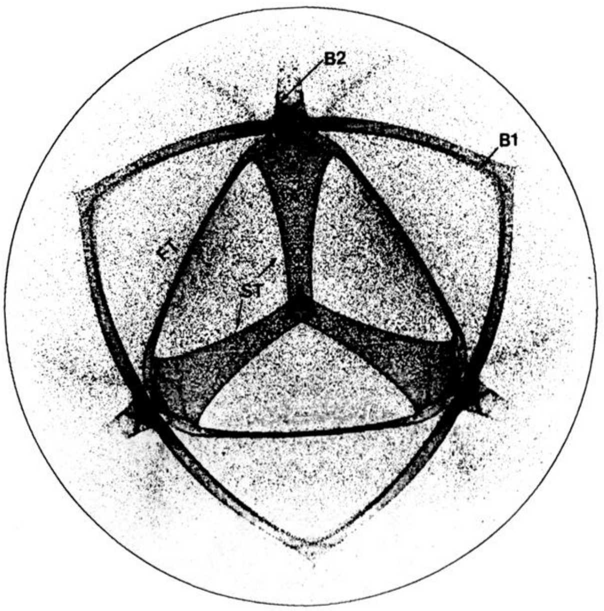

FIG. 17. Polar phonon-intensity diagram for the sapphire *XY* surface.

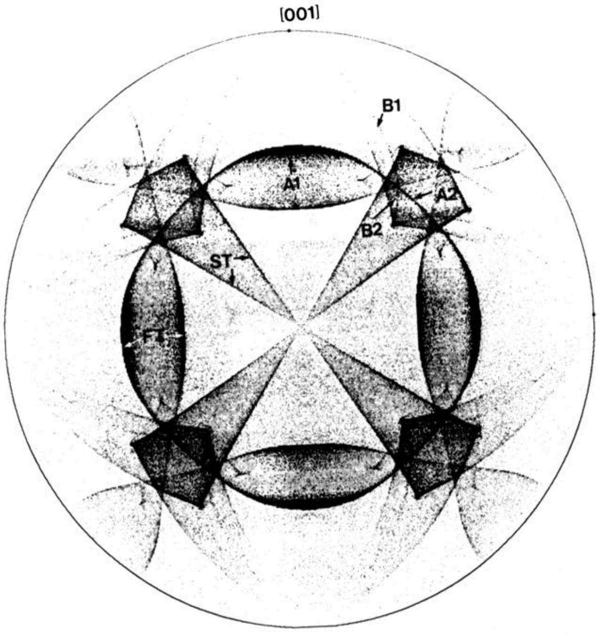

FIG. 19. Polar phonon-intensity diagram for CsCl(100).

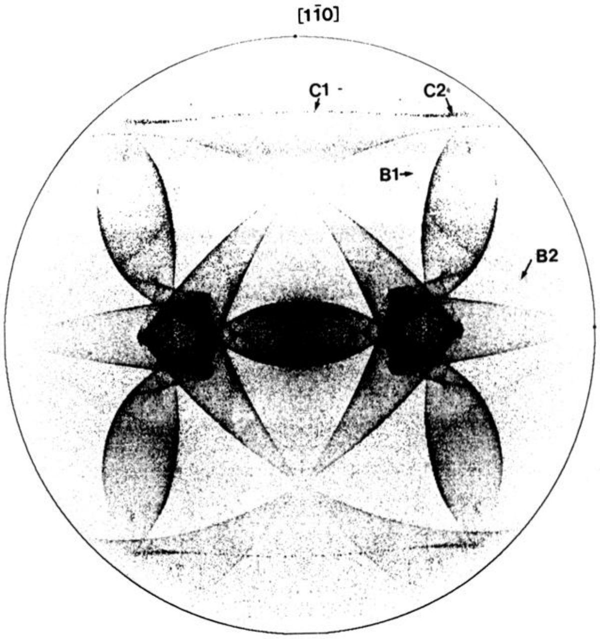

FIG. 21. Polar phonon-intensity diagram for CsCl(110).

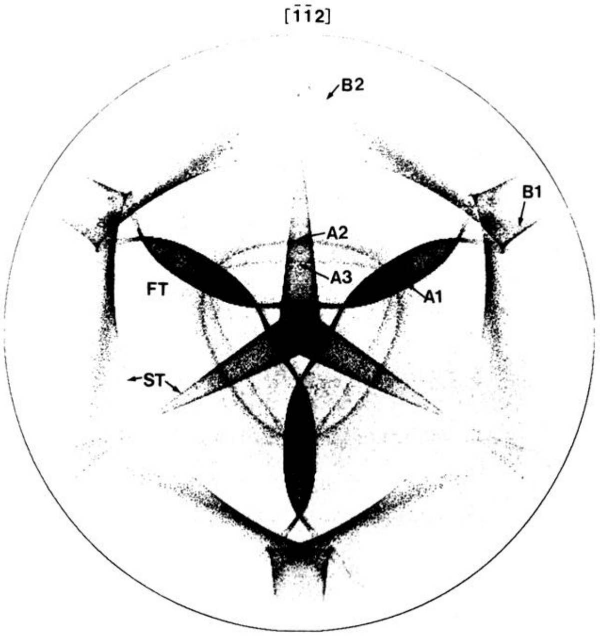

FIG. 23. Polar phonon-intensity diagram for NaF(111).

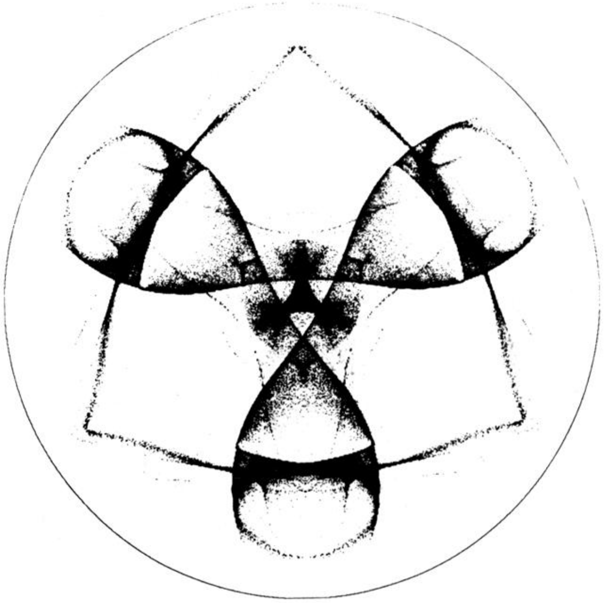

FIG. 24. Polar phonon-intensity diagram for the quartz *XY* surface. The elastic constants for the calculation are taken from Ref. 31.

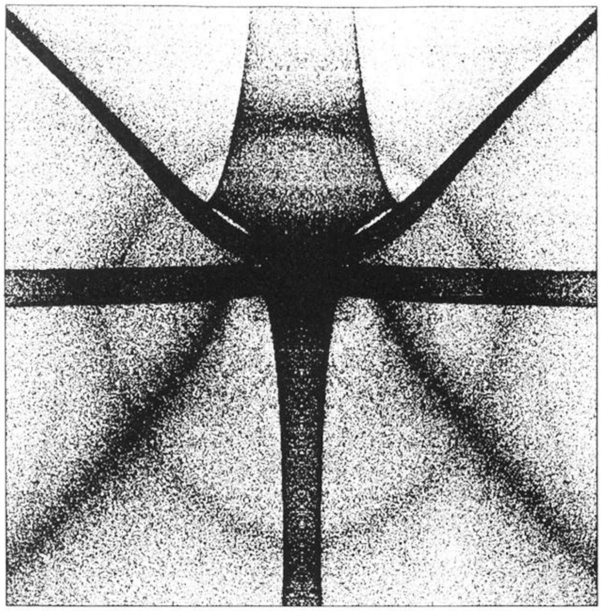

FIG. 5. Calculated phonon image for sapphire with ($\theta = 58°$, $\phi = 30°$) surface orientation. The horizontal and vertical half-angles of view are ±32°. Only the ST and FT phonon fluxes are displayed. Phonon intensity is represented by the darkness of the greyscale, which comes from the density of printing points. The elastic constants for the calculation are taken from Ref. 25.

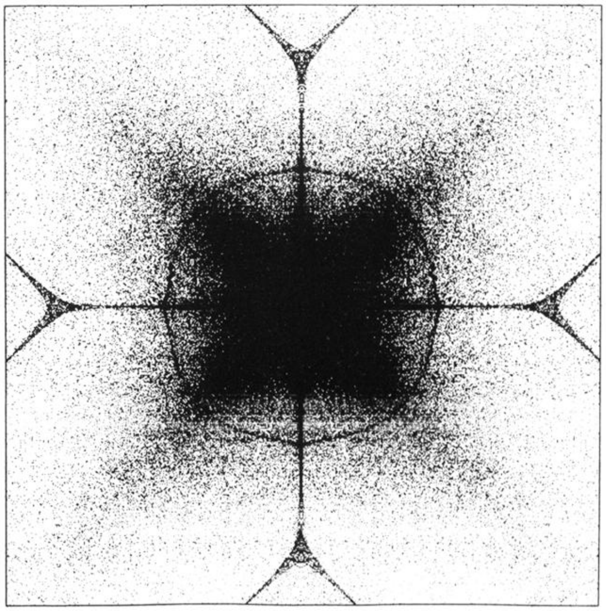

FIG. 6. Calculated phonon image for diamond with (100) surface orientation. Horizontal and vertical half-angles of view are ±60°. The [111] direction is in the center of the threefold structure near the top center of the image. The elastic constants for the calculation are taken from Ref. 26.

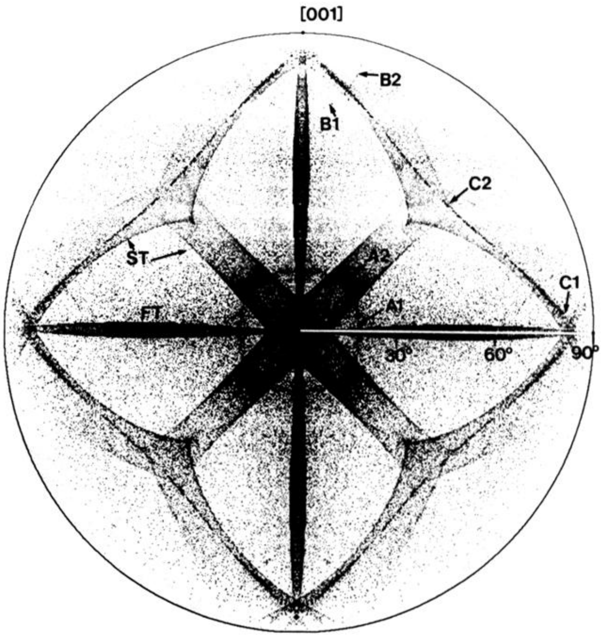

FIG. 9. Polar diagram of ST and FT phonon intensity for the (100) surface of Ge. Bulk-phonon-focusing caustics are identified by branch (ST or FT). Points labeled *A* 1, *A* 2, *B* 1, etc. on the PSW structures are mapped from similarly labeled points in Fig. 8.